Breakdown of the Wiedemann–Franz law in a unitary Fermi gas

Dominik Husmann[a], Martin Lebrat[a], Samuel Häusler[a], Jean-Philippe Brantut[b], Laura Corman[a,1], and Tilman Esslinger[a]

[a]Institute for Quantum Electronics, ETH Zurich, 8093 Zurich, Switzerland; and [b]Institute of Physics, École Polytechnique Fédérale de Lausanne, 1015 Lausanne, Switzerland

Edited by Wolfgang Ketterle, Massachusetts Institute of Technology, Cambridge, MA, and approved July 11, 2018 (received for review February 23, 2018)

We report on coupled heat and particle transport measurements through a quantum point contact (QPC) connecting two reservoirs of resonantly interacting, finite temperature Fermi gases. After heating one of them, we observe a particle current flowing from cold to hot. We monitor the temperature evolution of the reservoirs and find that the system evolves after an initial response into a nonequilibrium steady state with finite temperature and chemical potential differences across the QPC. In this state any relaxation in the form of heat and particle currents vanishes. From our measurements we extract the transport coefficients of the QPC and deduce a Lorenz number violating the Wiedemann–Franz law by one order of magnitude, a characteristic persisting even for a wide contact. In contrast, the Seebeck coefficient takes a value close to that expected for a noninteracting Fermi gas and shows a smooth decrease as the atom density close to the QPC is increased beyond the superfluid transition. Our work represents a fermionic analog of the fountain effect observed with superfluid helium and poses challenges for microscopic modeling of the finite temperature dynamics of the unitary Fermi gas.

cold atoms | mesoscopic physics | unitary Fermi gas | thermoelectric effects | quantum simulation

The interplay between heat and matter currents in a many-body system sheds light on its fundamental properties and the character of its excitations. Transport measurements are a particularly important probe in the presence of strong interactions and high temperatures T, when a microscopic model is absent or computationally intractable. Phenomenologically, the dependence of the currents on external biases is captured by transport coefficients, such as the particle conductance G or the thermal conductance G_T. They determine the ability of a system to relax toward equilibrium at long times and give unique information on its physical nature. For instance, the Wiedemann–Franz law states that the ratio $G_T/TG \equiv L$, the Lorenz number, takes a universal value for all Fermi liquids in the low-temperature limit. Therefore, any breakdown signals physics going beyond a Fermi liquid behavior, as has been observed in the normal phase of high-temperature superconductors (1). In addition, measuring the coupling between heat and particle currents, the Seebeck or Peltier effects, gives direct access to the entropy carried by one transported particle and sensitively probes the energy dependence of the transport processes. Numerous studies have documented the importance of such measurements (2, 3), both for realizing efficient thermoelectric materials (4) and for understanding correlated systems (5, 6).

A cold atomic Fermi gas in the vicinity of a Feshbach resonance is a fundamental example of a strongly correlated Fermi system. Owing to the control offered by laser manipulation, its trapping potential can be shaped into custom geometries such as a two-terminal configuration, allowing one to measure transport coefficients (7). Previous studies of the unitary Fermi gas have charted out its thermodynamic properties (8, 9). Recently, transport experiments have observed dissipation processes occurring in the presence of a weak link, such as vortex nucleation in a Josephson junction and multiple Andreev reflections (10–12), and heat waves in the form of second sound have been observed (13, 14).

Thermoelectric effects in cold atoms have been studied for bosonic systems (15–18) and within Bardeen–Cooper–Schrieffer (BCS) theory (19); however, the thermoelectric coupling between heat and particle currents in the unitary regime has not been experimentally addressed. Such a study is particularly relevant for applications to cooling protocols as well as for singling out the contribution of fermionic particles to heat flow (20–23). Indeed, in contrast to solid-state systems, where the lattice melts at high temperatures, the unitary Fermi gas realized in cold atoms remains free of lattice phonons at all temperatures.

In this paper, we report on measurements of heat and particle transport through a quantum point contact connecting two reservoirs of strongly correlated Fermi gases across the superfluid transition. We explore the unitary Fermi gas at temperatures slightly below the critical temperature, where the reservoirs are weakly in the superfluid regime. There we have observed a linear current–bias relation, contrary to lower-temperature regimes at a superfluid–normal–superfluid junction where nonlinearities have been shown (12). We enter the predicted large critical region of the normal-to-superfluid transition of the unitary Fermi gas (24) where the behavior of the many-body system still needs to be investigated. It is an open question whether the disappearance of the superfluid signature in particle transport is concomitant with a restored Fermi liquid behavior.

Significance

Heat and matter currents are required to relax an out-of-equilibrium system with temperature and chemical potential gradients to thermodynamical equilibrium. The ratio of heat to particle conductance characterizes this response and takes a universal value for typical electronic materials, known as the Wiedemann–Franz law, originating in the quasi-particle nature of the excitations contributing to transport. Investigating the transport dynamics between two reservoirs of ultracold and strongly interacting Fermi gases, connected by a quantum point contact, we observe a nonequilibrium steady state, strongly violating the Wiedemann–Franz law. This cold atom version of the fountain effect, previously observed in superfluid helium superleaks, is characterized by a weak coupling between heat and particle currents that results in a nonvanishing Seebeck coefficient.

Author contributions: D.H., M.L., S.H., J.-P.B., L.C., and T.E. designed research; D.H., M.L., S.H., and L.C. performed research; D.H., M.L., S.H., and L.C. analyzed data; and D.H., M.L., S.H., J.-P.B., L.C., and T.E. wrote the paper.

The authors declare no conflict of interest.

This article is a PNAS Direct Submission.

[1]To whom correspondence should be addressed. Email: lcorman@phys.ethz.ch.

This article contains supporting information online at www.pnas.org/lookup/suppl/doi:10.1073/pnas.1803336115/-/DCSupplemental.

Published online August 9, 2018.

We observe the evolution of an initially imposed temperature imbalance for equal atom numbers in a two-terminal Landauer configuration (7). In general, coupled particle and heat currents tend to pull a system toward thermodynamical equilibrium. However, here the system evolves toward a nonequilibrium steady state (NESS) within the timescale of the experiment. While typically a NESS is associated to stationary states of open systems (25), here it can also describe our experiments due to the presence of dissipation and thermodynamic driving forces. Our results sharply contrast with previous experiments observing heat transport with weakly interacting atoms (26). There a single time constant was found to describe the dynamics for temperature and particle relaxation.

Here, our observations reveal a strong separation of heat and particle transport timescales, resulting in a Lorenz number much lower than the value expected for a Fermi liquid. The paradigmatic system supporting suppressed heat transport is the so-called superleak in liquid bosonic helium II. Heating one side of the superleak yields the fountain effect, where both the Seebeck coefficient and the thermal conductance vanish. Our observations represent a fermionic analog to the fountain effect, where the quantum point contact (QPC) takes the role of the superleak with very low thermal and particle conductance in the noninteracting limit. We, however, measure a finite Seebeck coefficient even in the superfluid regime, calling for a description of the transport process going beyond the standard two-fluid model.

System

Our experiment consists of a QPC imprinted onto a cold, unitary Fermi gas of ^{6}Li atoms, as in our previous work (12, 27). We form the QPC using two far-detuned repulsive laser beams with a line of zero intensity in the center, resulting in a region of tight harmonic confinement with typical frequencies of $\nu_x = 20.2(6)$ kHz and $\nu_z = 12.9(5)$ kHz (Fig. 1*A*) setting an energy spacing between transverse modes of $h\nu_{x(z)}$. This mesoscopic structure connects two initially decoupled reservoirs, labeled as left (L) and right (R), and enables the transport of particles and heat. The reservoirs contain a mixture of the lowest and third lowest hyperfine state, with typically $N = N_\mathrm{L} + N_\mathrm{R} = 97(4)\cdot 10^3$ atoms in each spin state, temperatures of $\bar{T} = (T_\mathrm{L} + T_\mathrm{R})/2 = 184(8)$ nK, and chemical potentials of $\bar{\mu} = (\mu_\mathrm{L} + \mu_\mathrm{R})/2 = 272(24)\ \mathrm{nK}\cdot k_\mathrm{B}$. Here N_i, T_i, and μ_i with $i = \mathrm{L}, \mathrm{R}$ indicate the atom number, temperature, and chemical potential of the individual reservoirs. We control the density inside and close to the QPC by varying the power of an additional laser beam which creates an attractive gate potential V_G. At this temperature and chemical potential, up to a few transverse modes in the x and z direction are populated (*SI Appendix*, *Transport Modes*).

We bring the system out of equilibrium by heating either of the reservoirs using an intensity-modulated laser beam focused on the reservoir, while maintaining the QPC closed. This results in a temperature difference up to $\Delta T = T_\mathrm{L} - T_\mathrm{R} = \pm 83$ nK. In each of the reservoirs, seen as half-harmonic traps, atom number N and internal energy E are obtained from density profiles (Fig. 1*B*). These quantities can be converted to any other thermodynamic variable such as temperature T or chemical potential μ, using the unitary equation of state (EoS). Here the reduced chemical potential $q = \bar{\mu}/k_\mathrm{B}\bar{T} \approx 1.5$ in the reservoirs is below the superfluid transition point at $q_c = 2.5$ (14). By tuning the gate potential V_G the degeneracy can be increased in the vicinity of the QPC. The gate beam thus acts as a local dimple creating superfluid regions close to the QPC (*SI Appendix*, *Density Distribution in the Center*). We perform a transport experiment by opening the QPC for a variable time t between 0 s and 4 s and subsequently measuring $\Delta N(t)$ and $\Delta T(t)$. For convenience, we omit to write explicitly the time dependence of these quantities. Particle and heat exchange between the reservoirs is enabled during this time, leading to relaxation dynamics depicted in Fig. 1*C*.

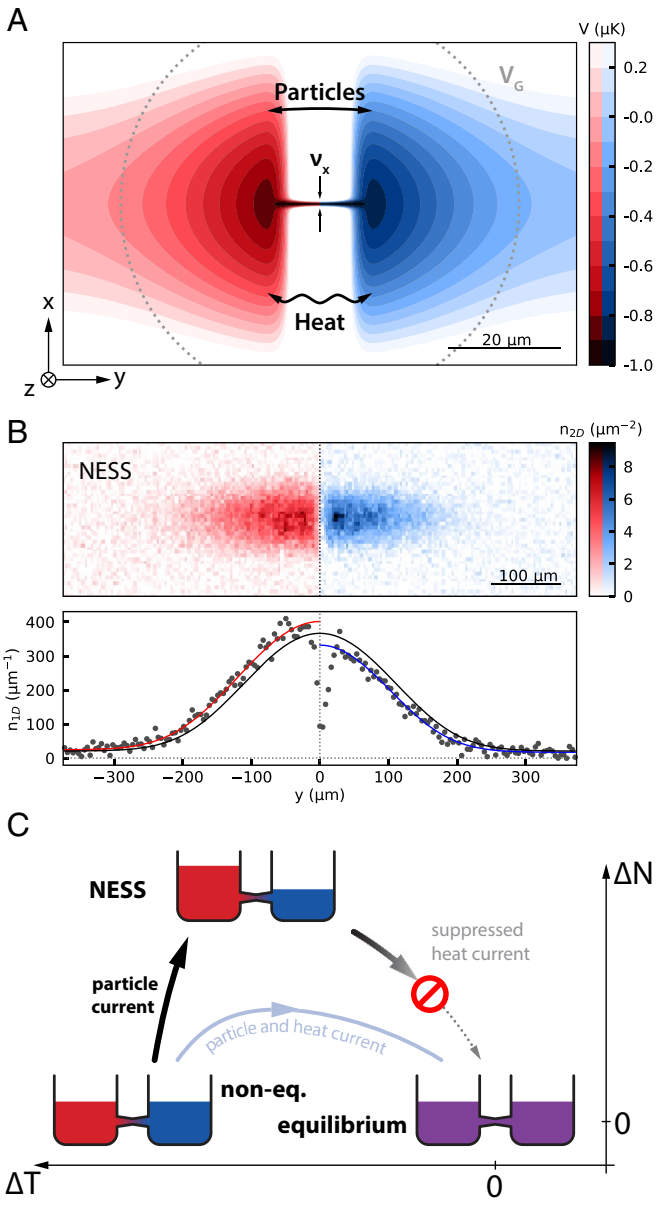

Fig. 1. (*A*) Particle and heat exchange between two reservoirs containing fermions with resonant interactions, mediated by the QPC which is characterized by the confinement frequencies ν_x and ν_z and a gate potential V_G. We indicate equipotential lines at the channel connecting the hot (red) and cold (blue) reservoirs. (*B*) Absorption picture and density profile after 1 ms of time of flight. Here, a NESS has been reached after 4 s of transport. Solid lines indicate fits (*SI Appendix*, *Thermodynamic Properties of the Reservoirs*), from which we deduce both the atom numbers $N_\mathrm{R} = 35(1)\cdot 10^3$, $N_\mathrm{L} = 51(1)\cdot 10^3$, and temperatures $T_\mathrm{R} = 163(9)$ nK and $T_\mathrm{L} = 231(8)$ nK. (*C*) Schematics of the thermodynamic equilibration process in (ΔT, ΔN) space with ΔT and ΔN increasing along the arrow direction. In general, a temperature-biased nonequilibrium state evolves toward thermodynamic equilibrium along a trajectory indicated in light blue. In the particular case of vanishing heat diffusion, the system evolves predominantly along the ΔN axis to a NESS where the absence of thermal relaxation processes prevents evolution to thermodynamic equilibrium.

Dynamics

Fig. 2 presents a typical time evolution of ΔN, $T_\mathrm{R,L}$, and $\Delta\mu$ during transport. The gate potential and transverse frequencies

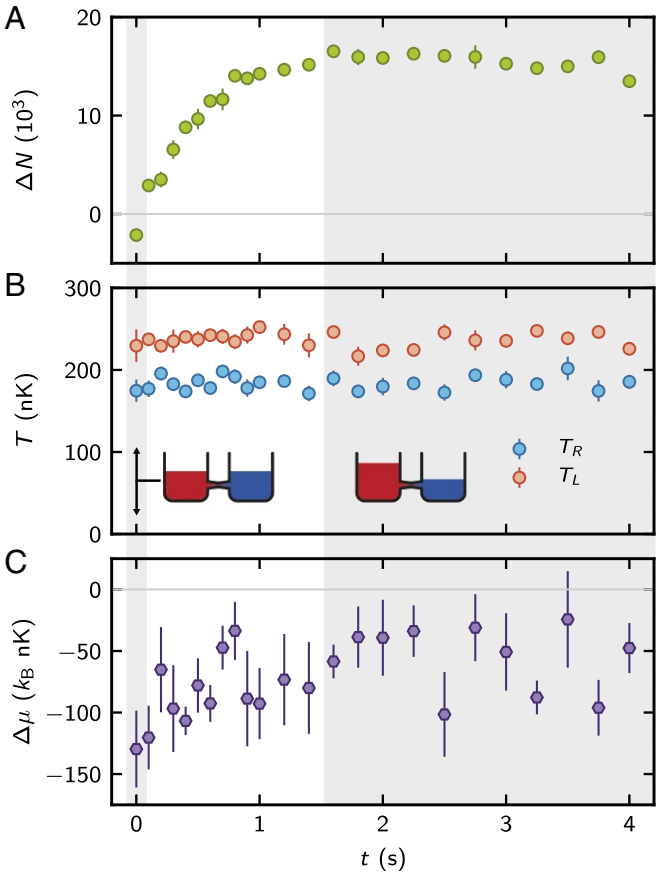

Fig. 2. (*A–C*) Evolution of particle number imbalance ΔN (*A*), temperatures in the left (red) and the right (blue) reservoir $T_{L,R}$ (*B*), and chemical potential bias $\Delta\mu$ (*C*) as a function of time t for an initial temperature imbalance of $\Delta T_0 = 49(8)$ nK. Within the first 1.5 s a particle imbalance builds up, while the temperature bias shows no measurable evolution. On the same timescale, $\Delta\mu$ decreases to a finite nonzero value, leading to a NESS with finite ΔN and $\Delta\mu$. In this configuration the high-density regions close to the QPC are superfluid with local reduced chemical potentials of $q_L = 3.2(4)$ on the left side and $q_R = 5.0(5)$ on the right side.

were set to $V_G = 1.00(3)$ μK$\cdot k_B$ and $\nu_x = 20.2(6)$ kHz, respectively. The high-density regions close to the QPC are superfluid in this configuration. The initial state was prepared with $\Delta T_0 = \Delta T(t=0) = 49(8)$ nK and $\Delta N_0 = 0$, with the equilibrium thermodynamics of the reservoirs yielding $\Delta\mu_0 = \mu_L - \mu_R \approx -130(31)$ nK$\cdot k_B$. During the first 1.5 s, a relative particle imbalance $\Delta N/N \approx 0.16(1)$ rapidly builds up, leading to a decrease of $|\Delta\mu|$ while ΔT is constant within experimental resolution. This evolution is driven by the finite value of $\Delta\mu$, resulting in a large current from the cold to the hot reservoir. It dominates over the much weaker thermoelectric current from the hot to the cold reservoir, originating from the energy dependence of the transmission through the QPC. This contrasts with previous observations with weakly interacting atoms (26, 28) where the thermoelectric current was the dominating contribution.

After a typical timescale τ_+, ΔT and ΔN reach a steady state, strongly departing from thermodynamical equilibrium. Interestingly, the decline in $\Delta\mu$ stops at a nonzero value $\Delta\mu_s \approx -55(8)$ nK$\cdot k_B$, which is estimated by taking the average over the data points for times $t \geq 1.6$ s. To account for the very weak decrease of ΔN in the second half of the observation time, we introduce a much longer timescale τ_- describing the decay of ΔN and ΔT back to zero. This timescale corresponds to the thermal equilibration process shown in Fig. 1*C*, and our observation shows that $\tau_- \gg \tau_+$.

To provide a quantitative understanding of the time evolution of the system, we use a phenomenological model based on linear response. While such an approach is known to fail in the lowest temperature regimes, where nonlinear current–bias relations have been observed (12), we find that it describes our observations well (*SI Appendix*, *Linear Model*) and allows for comparison between different QPC parameters. In this framework, the particle current $I_N = -1/2 \cdot \mathrm{d}\Delta N/\mathrm{d}t$ and entropy current $I_S = -1/2 \cdot \mathrm{d}\Delta S/\mathrm{d}t$ are expressed as a function of the differences in chemical potential $\Delta\mu$ and temperature ΔT between the reservoirs (28, 29):

$$\begin{pmatrix} I_N \\ I_S \end{pmatrix} = G \begin{pmatrix} 1 & \alpha_c \\ \alpha_c & L + \alpha_c^2 \end{pmatrix} \cdot \begin{pmatrix} \Delta\mu \\ \Delta T \end{pmatrix}. \quad [1]$$

The transport properties of the channel are captured by its particle and thermal conductances G and G_T, which can be combined into the Lorenz number $L = G_T/(\bar{T}G)$, and its Seebeck coefficient α_c describing the coupling between particle and entropy currents.

The absence of the relaxation of temperature and particle imbalance shown in Fig. 2 implies a very low heat conductance. According to the first law of thermodynamics the energy flow I_E can be expressed as

$$I_E = \bar{T} \cdot I_S + \bar{\mu} \cdot I_N = (\bar{\mu} + \alpha_c \bar{T}) I_N + G_T \Delta T, \quad [2]$$

where the first term on the right represents work flow and the second term heat flow. Work is associated with the reversible transfer of an average energy per particle $\bar{\mu} + \alpha_c \bar{T}$, while irreversible, diffusive heat transfer is proportional to ΔT, obeying Fourier's law. From Fig. 2*A*, we find $I_N = 0$ and $\Delta T > 0$ for longer times. A direct measurement of I_E yields a low value for the heat conductance of $G_T = 0.2 \cdot G_{T,\mathrm{NIF}}$, where $G_{T,\mathrm{NIF}}$ is the conductance expected for a noninteracting Fermi gas with the same chemical potential, temperature, and gate potential (*SI Appendix*, *Transport Coefficients in a Noninteracting System*).

Transport Coefficients

The transport parameters in mesoscopic systems strongly depend on the geometry of the channel (30). We investigate this dependency by measuring the dynamics of atom number difference and temperature difference as the channel confinement is reduced, departing from the single-mode regime. Fig. 3*A* presents the results for four different transverse confinements ν_x. For weaker confinements, ΔN and ΔT equilibrate to zero for long times. This is expected as the geometric contact between the two reservoirs increases in size, leading to higher particle and diffusive heat currents.

We fitted the time traces with the solutions from the linear response model in Eq. **1**, which are biexponential functions where we fixed $\Delta N(t=0) = 0$ and $\Delta T(t=0) = \Delta T_0$ according to our preparation:

$$\Delta N(t) = A[\exp(-t/\tau_+) - \exp(-t/\tau_-)] \quad [3]$$

$$\Delta T(t) = B\exp(-t/\tau_+) + (\Delta T_0 - B)\exp(-t/\tau_-). \quad [4]$$

The fit parameters τ_+, τ_-, A, and B are functions of the transport coefficients of the channel α_c, G, L and the thermodynamics of the reservoirs through their compressibility, heat capacity, and dilatation coefficient. The fit is performed simultaneously on both ΔN and ΔT, normalized with the statistical uncertainty of the data. We find two timescales τ_+ and τ_- that differ by one order of magnitude, a feature that remains even for fast equilibration at weak confinement (Fig. 3*B*). Consequently, each timescale can be mapped to the relaxation dynamics of heat (τ_-)

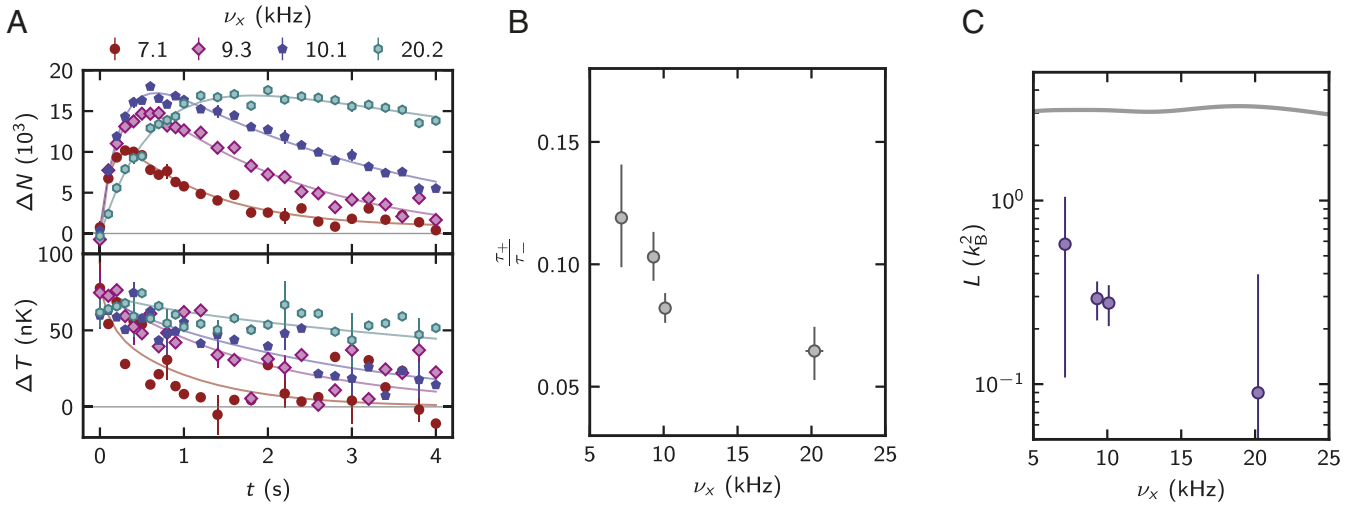

Fig. 3. Variation of the transverse confinement frequencies ν_x. (*A*) Evolution of ΔN and ΔT for confinements $\nu_x = 7.1(2)$ kHz, 9.3(3) kHz, 10.1(3) kHz, and 20.2(6) kHz for fixed $V_G = 1.00(3)$ $\mu K \cdot k_B$. For high confinement, the system evolves toward a NESS. A decrease in ν_x results in increased relaxation to thermodynamical equilibrium. Solid lines represent biexponential fits to the data (Eqs. **3** and **4**). Both the left and the right reservoir are in the superfluid phase with $q_L = 3.4(6)$ and $q_R = 5.9(7)$ at $t = 0$ s, where the values are averaged over the different confinements. Error bars indicate SEs for every fourth data point. (*B*) Ratio of the timescales τ_+, τ_- from biexponential fits for various values of the confinement. While both timescales increase with confinement, their ratio decreases, indicating a strong change in the transport coefficients for heat and particle transport. (*C*) Experimentally determined Lorenz number L (violet circles) and Lorenz number expected for an equivalent noninteracting system (gray line) at equal chemical potential and temperature. The measured values lie consistently below the $\pi^2/3 \cdot k_B^2$ predicted by Wiedemann–Franz law.

and particles (τ_+) (*SI Appendix*, *Linear Model*). Within this linear response solution, the direction and magnitude of the currents result from a competition between the transport properties of the channel and the thermodynamic response of the reservoirs (*SI Appendix*, *Linear Model*), a feature that was encountered already for the weakly interacting Fermi gas in ref. 26.

Lorenz Number. The relative weight of particle and heat conductance is captured by the Lorenz number L. Direct conversion of the fit parameters in Eqs. **3** and **4** to L is, however, not possible because the biexponential model is ill-conditioned. Instead we express L by estimating G and G_T from particle and energy currents I_N and I_E obtained from the data. The thermal conductance and Seebeck coefficient are given by $G_T = I_E/\Delta T$ and $\alpha_c = -\Delta\mu/\Delta T$ at the point of vanishing particle current (Eq. **1**). The conductance G is calculated for short transport times where we obtain $G = I_N/(\Delta\mu + \alpha_c \Delta T)$ (see *SI Appendix*, *Evaluation of Transport Parameters* for details).

The estimates of the Lorenz number are presented in Fig. 3*C*, together with the expected value for a noninteracting QPC obtained through Landauer theory with equivalent chemical potential, temperature, and channel properties (28). For all values of ν_x, L is much smaller than in the noninteracting case, which approaches the Wiedemann–Franz law $L_{WF} = \pi^2/3 \cdot k_B^2$. Our observations thus violate the Wiedemann–Franz law by an order of magnitude. This law roots in having the same carriers for charge and heat and is robust to moderate interactions, where the system can be described by a Fermi liquid. Deviations from this law may appear when Fermi liquid theory breaks down, as encountered for example in strongly correlated 1D systems, where the Lorenz number can either increase (5) or decrease (31–33). This is in line with our previous work, which showed that the conductance of the strongly interacting Fermi gas close to the critical point strongly differs from the predictions of the Landauer formula (12, 34).

Seebeck Coefficient. The NESS observed in Fig. 2 allows us to relate chemical potential and temperature differences to the Seebeck coefficient. Therefore we express the vanishing particle current as a competition between a current driven by $\Delta\mu$ and a current driven by ΔT. In the NESS, the two contributions compensate each other. From the NESS realized in Fig. 2, we find $\alpha_c = -\Delta\mu/\Delta T = 1.1(2) k_B$. Here we rely on a linear relation between the stationary value of ΔT and $\Delta\mu$ (Eq. **1**) at the times where particle current $I_N = 0$ vanishes (gray area in Fig. 2). We measured $(\Delta N, \Delta T)$ for different values of the heating (see Fig. 4*A* for time traces) and convert them to $(\Delta\mu, \Delta T)$.

For the specific case of $V_G = 1.00(3)$ $\mu K \cdot k_B$ and $\nu_x = 20.2(6)$ kHz, we characterize the quasi-steady state for a transport time of $t = 2$ s and find a linear relation between $\Delta\mu$ and ΔT (Fig. 4*B*). This confirms that the linear model Eq. **1** constitutes an adequate description of our system. The linear relation yields a Seebeck coefficient $\alpha_c = 1.2(2) k_B$. To check that the measurement of α_c does not depend on the precise value of the transport time, we repeat the measurement at $t = 4$ s and find consistent values. This value is very close to the case of a 1D quantum wire in the noninteracting regime, where one expects $\alpha_{NIF} = 1 k_B$ (*SI Appendix*, *Transport Coefficients in a Noninteracting System*). We further investigate the Seebeck coefficient by increasing the attractive gate potential V_G centered on the QPC. This method has two consequences on the two-terminal system: (*i*) It probes the single-particle energy dependence of the transport parameters by increasing the number of available modes in the QPC and (*ii*) the density in the vicinity of the QPC is modified by tuning the chemical potential, locally increasing the superfluid gap. We measure $\Delta\mu$ and ΔT for various heating strengths when $I_N = 0$ as in Fig. 4*B* and deduce α_c.

Fig. 4*C* shows α_c as a function of the chemical potential modified by the attractive gate $\tilde{\mu} = \bar{\mu} + V_G$. The Seebeck coefficient decreases from a value slightly below $2k_B$ at $\tilde{\mu} = 0.91(3)$ $\mu K \cdot k_B$ to a value close to zero for $\tilde{\mu} > 2.06(6)$ $\mu K \cdot k_B$. A similar decrease of α_c is theoretically expected for a noninteracting QPC (black curve in Fig. 4*C*) and is explained there by an increase of the number of 1D channels available for the transport of single particles. This similarity is surprising as transport coefficients in this regime close to the superfluid transition have shown order of magnitude deviations from the Landauer model (12, 34). The residual deviation from the noninteracting

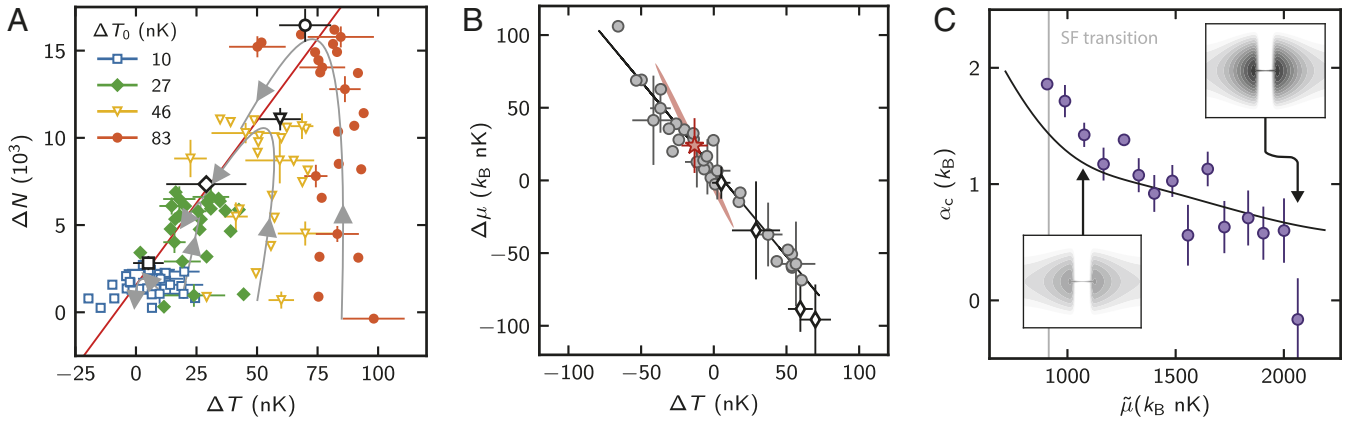

Fig. 4. (*A*) Transients in (ΔT, ΔN) space for various values of initial heating $\Delta T_0 = 10(5)$ nK, 27(7) nK, 46(8) nK, and 83(7) nK at fixed $\nu_x = 20.2(6)$ kHz and $V_G = 1.00(3)$ $\mu K \cdot k_B$. Gray lines are fits with Eqs. **3** and **4** for $t = 0-8$ s, where the arrows indicate the time progress. The NESS is at different stopping points (black) depending on the initial heating. Error bars indicate SEs for every fourth data point. (*B*) Detailed study of $\Delta\mu$ vs. ΔT (gray circles) at $t = 2$ s, where particle current is zero. The black line indicates a linear fit to the data, with the slope representing the Seebeck coefficient $d\Delta\mu/d\Delta T = -\alpha$. Included in the fits is the covariance of the data points, shown by the red shaded region for a selected data point (red star) representative for the full dataset (for details on the fit see *SI Appendix, Evaluation of Transport Parameters*). The four stopping points from *A* are indicated as black diamonds. Error bars indicate SEs for every fourth data point. (*C*) Measurement of the Seebeck coefficient for various values of the gate potential V_G. The black line shows the prediction for an equivalent noninteracting system (equal temperature and chemical potential). The transition point in the pockets from normal to superfluid is indicated as a gray line.

curve—manifested in the faster decrease with $\tilde{\mu}$—is compatible with the expectations for a BCS superfluid close to the transition point, where a smooth decrease of α_c from the noninteracting value to zero is expected (35).

Discussion

The coexistence of a vanishing Lorenz number and a finite Seebeck coefficient leading to a NESS at finite $\Delta\mu$ distinguishes our observations from the fountain effect seen in superfluid helium II (36, 37). There, two vessels are connected by a macroscopic duct, called a superleak. Heating one of them induces a current from cold to hot until a steady state with different temperatures and pressures is reached. In a two-fluid description of the superleak, viscosity prevents the normal, entropy-carrying fraction of the fluid from crossing while allowing the entropy-less, superfluid fraction to flow and equilibrate the chemical potentials, $\Delta\mu = 0$ (15, 19). On the contrary, our system is characterized by a nonzero Seebeck coefficient $\alpha_c = I_S/I_N$ in the limit $L = 0$, indicating a mean entropy transported by each particle of about $1k_B$. In addition, our QPC is ballistic and not diffusive, and both its high resistance for a normal Fermi gas (27) and its low resistance for a superfluid (12) are predominantly determined by quantum effects. The hydrodynamic models describing the fountain effect are therefore expected to break down. Although thermoelectric transport across a Josephson junction is well understood within BCS theory (35, 38), no model has so far been proposed to describe the unitary Fermi gas at a QPC.

The nonvanishing α_c associated with a low Lorenz number suggests that our QPC considered as a thermoelectric device has a high efficiency. Within this framework, the time evolution of the reservoirs describes an open thermodynamic cycle. There, the system acts first as a thermoelectric cooler, where a chemical potential difference drives convection heat from the cold to the hot reservoir, followed by a thermoelectric engine part, where the temperature difference drives particles from a lower to a higher chemical potential and hence produces work. As the transverse confinement frequency ν_x is increased, both processes slow down and evolution gets closer to reversibility, resulting in a decrease of the output power $P = I_N\Delta\mu$ and in a better conversion efficiency between work and heat. This efficiency is determined by a dimensionless figure of merit $ZT = \alpha_c^2/L$ (29) which is on the order of 14(8) for the largest confinement $\nu_x = 20.2(6)$ kHz, where the large errors stem from uncertainty in ΔT and $\Delta\mu$. Currently the best thermoelectric materials have figures of merit on the order of 3–5 (4, 39). Further considerations on the efficiency are given by the comparison with the Carnot efficiency (*SI Appendix, Efficiency*).

Our fountain effect setting with fermions provides a conceptual link between the thermoelectric transport witnessed in electronic devices and the bosonic fountain effect observed with helium II. Its anomalous features—exceptionally small Lorenz number and finite Seebeck coefficient—shed light on the out-of-equilibrium properties of the unitary Fermi gas and portend potential applications to ultracold atoms, such as the realization of novel cooling schemes. They also underline the necessity of a better understanding of strongly correlated systems at finite temperatures. Here, measuring the spin degree of freedom could yield additional information (20, 21), but the inhomogeneous nature of the system makes the interpretation even more challenging. A complementation to our present study would be the probing the full Bose–Einstein condensate (BEC)-BCS crossover. This, however, requires knowledge of the full finite temperature EoS, which has not been measured yet.

Materials and Methods

Preparing the Cloud and QPC. We prepare an elongated cloud of fermionic ^{6}Li atoms in a balanced mixture of the lowest and third lowest hyperfine state in a hybrid configuration of a far-detuned 1,064-nm dipole trap and a harmonic magnetic trap, confining the atoms along the transverse (*x*, *z*) and longitudinal (*y*) direction, respectively. We evaporatively cool down the cloud by reducing the trap depth from 6 μK to 3 μK on a broad Feshbach resonance at 689 G. After a final tilt evaporation step (40) along the *z* direction, the cloud reaches final temperatures of around 184(8) nK. The trap frequencies during transport are $\nu_{rx} = 318.5$ Hz, $\nu_{ry} = 28.4$ Hz, and $\nu_{rz} = 255.9$ Hz. A repulsive light-sheet beam at 532 nm created by a π-phase plate confines the cloud in the center in the *z* direction with a longitudinal $1/e^2$ waist of $w_{Ls,y} = 30(1)$ μm. An orthogonal 532-nm beam of waist $w_x = 5.49(1)$ μm in a split-gate shape with an intensity node in the center, realized with a transmission mask imaged onto the atom plane, confines the atoms in the *x* direction. The two transverse confinements effectively lead to a quasi-1D constriction with trapping frequencies $\nu_x = 20.2(6)$ kHz and $\nu_z = 12.9(5)$ kHz.

Transport. An amplitude-modulated beam at a wavelength of 767 nm is directed on one of the reservoirs, parametrically heating it up. The

modulation frequency is optimized experimentally to $\nu_{\mathrm{mod}} = 125$ Hz, which is on the order of the transverse trapping frequencies ν_{rx} and ν_{rz} of the dipole trap. The position of this beam is controlled by a piezo-steered mirror and can be shifted to either reservoir. The same beam is centered on the QPC during transport and acts there as an attractive gate potential V_G, locally tuning the density. When preparing the reservoirs, transport between the reservoirs is blocked by a repulsive wall beam focused onto the channel. The beam is removed for a variable transport time t during which exchange between the reservoirs through the channel is enabled. After time t we separate the reservoirs with the wall beam and take absorption images after a short time of flight of 1 ms in the transverse directions. This reduces the densities and allows us to image in the low saturation regime.

Thermodynamic Properties of the Reservoirs. From the density profiles we deduce the atom number in each reservoir as well as their internal energy $E = 3m(2\pi\nu_{ry})^2 \left\langle y^2 \right\rangle$ via the virial theorem for a harmonic trap at unitarity (41) and the second moment

$$\left\langle y^2 \right\rangle = \frac{\int_{-\infty}^{\infty} \mathrm{d}y n_{1\mathrm{D}}(y) y^2}{\int_{-\infty}^{\infty} \mathrm{d}y n_{1\mathrm{D}}(y)} \qquad [5]$$

of the fitted density distribution n_{1D} along the longitudinal direction (42) shown in Fig. 1*B*.

Along with the known equation of state of the unitary Fermi gas, these two quantities define all of the thermodynamic parameters of the individual reservoirs, including their temperatures $T_{\mathrm{L,R}}$ used in Figs. 2–4. The equation of state is based on measurements in ref. 8 and continued toward the normal and degenerate regimes in ref. 14 for a homogeneous gas. We apply local density approximation to obtain the trap-averaged quantities assuming a harmonic potential (*SI Appendix, Thermodynamic Properties of the Reservoirs*).

ACKNOWLEDGMENTS. We thank H. Aoki, A. Georges, T. Giamarchi, L. Glazman, D. Papoular, S. Pershoguba, S. Uchino, and W. Zwerger for discussions; B. Frank for providing the data on the superfluid gap; and B. Braem and P. Fabritius for careful reading of the manuscript. We acknowledge financing from the Swiss National Science Foundation under division II (Project 200020_169320 and National Centre of Competence in Research-Quantum Science and Technology); the Swiss State Secretary for Education, Research and Innovation Contract 15.0019 (Quantum Simulations of Insulators and Conductors); European Research Council (ERC) Advanced Grant TransQ (Mass, Heat and Spin Transport in Interlinked Quantum Gases) (Project 742579); and Army Research Office Multidisciplinary University Research Iniviative program Non-equilibrium Many-body Dynamics Grant W911NF-14-1-0003 for funding. J.-P.B. is supported by the ERC Starting Grant DECCA (Devices, Engines and Circuits: Quantum Engineering with Cold Atoms) (Project 714309) and the Sandoz Family Foundation–Monique de Meuron Program for Academic Promotion. L.C. is supported by an ETH Zurich Postdoctoral Fellowship and the Marie Curie Actions for People Cofunding of Regional, National and International Programmes.

1. Hill RW, Proust C, Taillefer L, Fournier P, Greene RL (2001) Breakdown of Fermi-liquid theory in a copper-oxide superconductor. *Nature* 414:711–715.
2. He J, Tritt TM (2017) Advances in thermoelectric materials research: Looking back and moving forward. *Science* 357:eaak9997.
3. Benenti G, Casati G, Saito K, Whitney R (2017) Fundamental aspects of steady-state conversion of heat to work at the nanoscale. *Phys Rep* 694:1–124.
4. Snyder GJ, Toberer ES (2008) Complex thermoelectric materials. *Nat Mater* 7:105–114.
5. Wakeham N, et al. (2011) Gross violation of the Wiedemann–Franz law in a quasi-one-dimensional conductor. *Nat Commun* 2:396.
6. Wang Y, Rogado NS, Cava RJ, Ong NP (2003) Spin entropy as the likely source of enhanced thermopower in $Na_xCo_2O_4$. *Nature* 423:425–428.
7. Krinner S, Esslinger T, Brantut JP (2017) Two-terminal transport measurements with cold atoms. *J Phys Condens Matter* 29:343003.
8. Ku MJH, Sommer AT, Cheuk LW, Zwierlein MW (2012) Revealing the superfluid lambda transition in the universal thermodynamics of a unitary Fermi gas. *Science* 335:563–567.
9. Nascimbène S, Navon N, Jiang KJ, Chevy F, Salomon C (2010) Exploring the thermodynamics of a universal Fermi gas. *Nature* 463:1057–1060.
10. Burchianti A, et al. (2018) Connecting dissipation and phase slips in a Josephson junction between fermionic superfluids. *Phys Rev Lett* 120:025302.
11. Valtolina G, et al. (2015) Josephson effect in fermionic superfluids across the BEC-BCS crossover. *Science* 350:1505–1508.
12. Husmann D, et al. (2015) Connecting strongly correlated superfluids by a quantum point contact. *Science* 350:1498–1501.
13. Sidorenkov LA, et al. (2013) Second sound and the superfluid fraction in a Fermi gas with resonant interactions. *Nature* 498:78–81.
14. Hou YH, Pitaevskii LP, Stringari S (2013) First and second sound in a highly elongated Fermi gas at unitarity. *Phys Rev A* 88:043630.
15. Karpiuk T, Grémaud B, Miniatura C, Gajda M (2012) Superfluid fountain effect in a Bose-Einstein condensate. *Phys Rev A* 86:033619.
16. Rançon A, Chin C, Levin K (2014) Bosonic thermoelectric transport and breakdown of universality. *New J Phys* 16:113072.
17. Papoular D, Pitaevskii L, Stringari S (2014) Fast thermalization and Helmholtz oscillations of an ultracold Bose gas. *Phys Rev Lett* 113:170601.
18. Filippone M, Hekking F, Minguzzi A (2016) Violation of the Wiedemann-Franz law for one-dimensional ultracold atomic gases. *Phys Rev A* 93:011602.
19. Sekera T, Bruder C, Belzig W (2016) Thermoelectricity in a junction between interacting cold atomic Fermi gases. *Phys Rev A* 94:033618.
20. Wong CH, Stoof HTC, Duine RA (2015) Spin-heat relaxation and thermospin diffusion in atomic Bose and Fermi gases. *Phys Rev A* 91:043602.
21. Kim H, Huse DA (2012) Heat and spin transport in a cold atomic Fermi gas. *Phys Rev A* 86:053607.
22. Grenier C, Georges A, Kollath C (2014) Peltier cooling of fermionic quantum gases. *Phys Rev Lett* 113:200601.
23. Papoular DJ, Ferrari G, Pitaevskii LP, Stringari S (2012) Increasing quantum degeneracy by heating a superfluid. *Phys Rev Lett* 109:084501.
24. Debelhoir T, Dupuis N (2016) Critical region of the superfluid transition in the BCS-BEC crossover. *Phys Rev A* 93:023642.
25. Labouvie R, Santra B, Heun S, Ott H (2016) Bistability in a driven-dissipative superfluid. *Phys Rev Lett* 116:235302.
26. Brantut JP, et al. (2013) A thermoelectric heat engine with ultracold atoms. *Science* 342:713–715.
27. Krinner S, Stadler D, Husmann D, Brantut JP, Esslinger T (2015) Observation of quantized conductance in neutral matter. *Nature* 517:64–67.
28. Grenier C, Kollath C, Georges A (2016) Thermoelectric transport and Peltier cooling of cold atomic gases. *Comptes Rendus Physique* 17:1161–1174.
29. Goupil C, Seifert W, Zabrocki K, Müller E, Snyder GJ (2011) Thermodynamics of thermoelectric phenomena and applications. *Entropy* 13:1481–1517.
30. Imry Y (2002) *Introduction to Mesoscopic Physics* (Oxford Univ Press, Oxford, NY).
31. Lee S, et al. (2017) Anomalously low electronic thermal conductivity in metallic vanadium dioxide. *Science* 355:371–374.
32. Bruin JAN, Sakai H, Perry RS, Mackenzie AP (2013) Similarity of scattering rates in metals showing t-linear resistivity. *Science* 339:804–807.
33. Hartnoll SA (2015) Theory of universal incoherent metallic transport. *Nat Phys* 11:54–61.
34. Krinner S, et al. (2016) Mapping out spin and particle conductances in a quantum point contact. *Proc Natl Acad Sci USA* 113:8144–8149.
35. Guttman GD, Nathanson B, Ben-Jacob E, Bergman DJ (1997) Thermoelectric and thermophase effects in Josephson junctions. *Phys Rev B* 55:12691–12700.
36. Allen JF, Misener AD (1938) Flow of liquid helium II. *Nature* 141:75.
37. Kapitza P (1938) Viscosity of liquid helium below the *lambda*-point. *Nature* 141:74.
38. Giazotto F, Martínez-Pérez MJ (2012) The Josephson heat interferometer. *Nature* 492:401–405.
39. Tan G, et al. (2016) Non-equilibrium processing leads to record high thermoelectric figure of merit in PbTe–SrTe. *Nat Commun* 7:12167.
40. Hung CL, Zhang X, Gemelke N, Chin C (2008) Accelerating evaporative cooling of atoms into Bose-Einstein condensation in optical traps. *Phys Rev A* 78:011604.
41. Thomas JE, Kinast J, Turlapov A (2005) Virial theorem and universality in a unitary Fermi gas. *Phys Rev Lett* 95:120402.
42. Guajardo ERS, Tey MK, Sidorenkov LA, Grimm R (2013) Higher-nodal collective modes in a resonantly interacting Fermi gas. *Phys Rev A* 87:063601.